RSC Advances

ROYAL SOCIETY OF CHEMISTRY

PAPER

View Article Online
View Journal | View Issue

Check for updates

Cite this: *RSC Adv.*, 2025, **15**, 22311

Fabrication and structural analysis of CuO–NiO and MWCNTs@CuO–NiO hybrid nanostructures: versatile materials for environmental and biomedical remediation

Amjad Latif Lone,[a] Sadiq Ur Rehman,[a] Sirajul Haq,*[a] Afrah F. Alkhuriji,[b] Nawal M. Al-Malahi,[b] Jamoliddin Razzokov,[cde] Shafia Shujaat[a] and Abdus Samad[f]

Received 8th April 2025
Accepted 12th June 2025

DOI: 10.1039/d5ra02443a

rsc.li/rsc-advances

This research focuses on the fabrication and characterization of a CuO–NiO nanocomposite (NC) and MWCNT-modified CuO–NiO NC for photocatalytic, antibacterial, and antioxidant applications. The bimetallic CuO–NiO nanostructure was fabricated *via* the sol–gel method and subsequently functionalized with multi-walled carbon nanotubes (MWCNTs). Various physicochemical techniques were employed to explore the structural, optical, and compositional characteristics of the prepared samples. The photocatalytic performance of the nanocomposites was assessed through the degradation of rhodamine 6G under solar-light irradiation. The MWCNTs@CuO–NiO NC demonstrated the highest removal efficiency of 95.37%, with a decomposition rate constant of 5.99312 min^{-1}. Their antibacterial efficacy was evaluated against two bacterial strains, namely, *E. coli* and *S. aureus*, and it was found that *E. coli* exhibited higher resistance to the samples. Furthermore, the MWCNTs@CuO–NiO NC demonstrated superior antioxidant activity compared with its bare counterpart, with an IC_{50} value of 84.61 µg mL^{-1}. The MWCNTs@CuO–NiO NC exhibited significantly enhanced antibacterial and antioxidant activities compared with the standard drug and pristine CuO–NiO NC. These findings highlight the multifunctional capabilities of the CuO–NiO NC and MWCNTs@CuO–NiO NC for environmental and biomedical applications.

1 Introduction

Environmental pollution refers to the unregulated release of mass or energy into Earth's natural environment, such as air, land, or water, which degrades the ecological balance over short or long periods, negatively impacting the quality and quantity of life.[1] One of the biggest issues facing the world today is environmental pollution.[2] According to a UNESCO report presented on behalf of UN-Water at the UN 2023 Water Conference in New York, approximately 2 billion people—equivalent to 26% of the global population—lack access to safe drinking water, while environmental contamination continues to worsen water pollution.[3] The extensive use of organic pollutants such as dyes and phenolic compounds by industries, including the textile, paper, chemical, pharmaceutical, paint, leather, food, and plastic industries, causes serious environmental deterioration, especially water contamination.[4] The primary contaminants in water resources are organic dyes.[5] Major illnesses including lower respiratory tract infections (20%), typhoid fever (8%), paratyphoid fever (20%) as well as acute and chronic gastrointestinal disorders are associated with water pollution. Diarrheal diseases account for 70% of water contamination-related mortality.[6] The highly fluorescent dye rhodamine 6G (R6G), a member of the rhodamine family, exhibits a good absorption coefficient, photostability, and water solubility. It is widely used in textiles, paper, cosmetics, and laser technologies. However, owing to its inefficient industrial wastewater treatment, it frequently contaminates aquatic ecosystems and is classified as a group 3 carcinogen, causing DNA damage, respiratory disorders and kidney/liver toxicity.[7] The formation of an effective treatment plan against rhodamine 6G is thus crucial as it is a highly hazardous substance.[8]

Antimicrobial resistance (AMR), primarily driven by the excessive and improper use of antibiotics, refers to the ability of microorganisms to survive and grow despite the presence of

---

[a] *Department of Chemistry, University of Azad Jammu and Kashmir, Muzaffarabad 13100, Pakistan. E-mail: cii_raj@yahoo.com*

[b] *Department of Zoology, College of Science, King Saud University, P. O. Box 2455, Riyadh, 11451, Saudi Arabia*

[c] *Institute of Fundamental and Applied Research, National Research University TIIAME, Kori Niyoziy 39, 100000 Tashkent, Uzbekistan*

[d] *Department of Chemical Engineering and Biotechnology, Karshi State Technical University, Mustaqillik Avenue street 225, 180100 Kashkadarya, Uzbekistan*

[e] *Department of Biotechnology, Tashkent State Technical University, Universitet 2, Tashkent 100095, Uzbekistan*

[f] *School of Material Science and Engineering, Nanjing Tech University, P. R. China*

antimicrobial drugs.[9] Multi-drug resistant (MDR) strains of numerous bacteria are distributed worldwide, and the WHO has listed this in the top ten global public health risks that lead to around 1.27 million deaths per year.[10] Clearly, antibiotic resistance, which has a significant influence on the clinical and economic fronts, is one of the major health issues in today's world.[11] There is a critical need for novel therapeutics to combat these MDR strains.[12]

Free radicals are highly reactive molecules with unpaired electrons that cause oxidative stress when overproduced, damaging cellular components and contributing to chronic diseases, like cancer and diabetes.[13–15] To counter these effects, advanced nanomaterials, such as bimetallic nanoparticles (BMNPs) and metal oxide nanoparticles (MONPs, *e.g.*, CuO, ZnO, Fe_2O_3) are attracting attention for their synergistic properties, including antioxidant, catalytic, and antibacterial capabilities.[16] Additionally, carbon nanotubes (CNTs) show promise in wastewater treatment by adsorbing organic pollutants.[17] These nanomaterials also serve as carriers for antimicrobial agents, highlighting their dual role in biomedical and environmental applications.[18] Their unique traits (*e.g.*, high surface area, magnetic/optical properties) make them versatile tools for addressing health and sustainability challenges.[19]

CuO (p-type) and NiO (n-type) form a p–n heterojunction, enhancing charge separation and reducing electron–hole recombination, which is critical for photocatalytic efficiency.[20] The combined bandgap (∼1.5–3.5 eV) allows broad solar-light absorption (visible to UV range), unlike single-metal oxides (*e.g.*, TiO_2, limited to UV). Furthermore, the release of dual metal ions (Cu^{2+}/Ni^{2+}) disrupts bacterial membranes and generates reactive oxygen species (ROS), offering broader-spectrum activity than Ag or ZnO NPs alone.[21,22] Unlike antibiotics, metal ions target multiple bacterial pathways simultaneously, minimizing resistance development. Moreover, MWCNTs act as electron highways, accelerating charge separation and prolonging carrier lifetimes, which boosts photocatalytic dye degradation compared to bare CuO–NiO. They also act as capping agents that prevent the aggregation of the CuO–NiO, while the N/S dopants provide additional binding sites that further enhance the ROS generation. Thus, the MWCNTs and CuO–NiO have a synergistic ability to lessen oxidative stress, and enhance the antioxidant photocatalytic, antifungal, anti-inflammatory, and antibacterial properties.[23] Recently, He *et al.* disclosed the fabrication of $CoSe_2/FeSe_2$-CNT NC *via* a hydrothermal process and demonstrated the efficacy of the NC as a photocatalyst for degrading various pollutants, including trimethoprim, levofloxacin, and ciprofloxacin. That study achieved the complete removal of levofloxacin within 10 min, while a mixed pollutant matrix required 120 min for degradation.[24]

The aim of the present study was to synthesize a multifunctional nanomaterial by integrating MWCNTs with a CuO–NiO NC, with an aim to simultaneously address environmental and biomedical challenges through the enhanced photocatalytic degradation of Rh-6G, broad-spectrum antibacterial activity (against Gram ± bacteria), and antioxidant properties, while aligning with the UN's Sustainable Development Goals 3 (good health) and 6 (clean water).

For this purpose, a modified sol–gel method was employed for the production of the CuO–NiO NC and MWCNT-modified CuO–NiO NC, which was an enhanced version of the traditional sol–gel process. This method is highly versatile as modifications were introduced in it to improve the properties of the final nanomaterials. The modified sol–gel method represents an efficient, faster, and more straightforward approach for synthesizing NCs, especially bimetallic oxide nanoparticles (BMONPs) and carbon nanotube (CNT)-modified BMONPs. The use of photocatalysis and agar-well diffusion for the removal of pollutants and for retarding the bacterial growth offer distinct advantages over conventional methods for pollutant degradation and antibacterial applications. Unlike chemical oxidation (*e.g.*, H_2O_2/Cl_2), which generates toxic byproducts, and merely transfers contaminants without degradation, creating disposal challenges, photocatalysis mineralizes organic dyes into harmless compounds *via* $^{\bullet}$OH and ROS generation, thereby aligning with green chemistry principles. Agar-well diffusion, though limited to qualitative antibacterial screening, provides visual inhibition zones for bacteria, complementing photocatalysis' broader microbial-killing capability. Meanwhile, traditional UV disinfection effectively inactivates pathogens but lacks residual action and fails to degrade chemical pollutants.

2 Experimental section

2.1 Reagents

This research project utilized only high-purity compounds throughout. The following materials were brought from Sigma Aldrich: methanol, sodium hydroxide, sodium dodecyl sulphate (SDS), nickel(II) nitrate hexahydrate, copper(II) nitrate pentahemihydrate, and diammonium salt (ABTS). The MWCNTs were functionalized with carboxylic group after being purchased from Sigma Aldrich. Utilizing deionized water (DIW), a working solution was created. After giving the glasses a thorough wash in DIW, acetone was used to rinse them. The glassware was used to create NCs after being dried in a thermal environment at 100 °C.

2.2 Synthesis CuO–NiO NC

Nickel(II) nitrate hexahydrate (4.55 g) and copper(II) nitrate pentahemihydrate (3.66 g) were separately dissolved in 10 mL of deionized water under continuously stirring for 30 min. Water-based solutions of CuO and NiO were mixed and heated at 60 °C for 30 min with vigorous stirring in a beaker. Meanwhile, 0.154 g of MWCNTs were ultrasonically dispersed in 100 mL of distilled water, and 10 mL of this dispersion was added to the reaction mixture containing the previously prepared metal solutions. The produced mixture was continuously stirred and heated at 60 °C for 3 h after adding 1 M sodium hydroxide solution until the pH was adjusted to 10. The reaction mixture was filtered and rinsed three times with DIW after being allowed to cool at room temperature for a full day. The resulting solid residue was calcined at 350 °C for 4 h in a muffle furnace and stored in an air-tight glass bottle.

2.3 Synthesis of MWCNT-modified CuO–NiO NC

In order to create MWCNTs@CuO–NiO NC, 3.66 g of copper(II) nitrate pentahemihydrate and 4.55 g of nickel(II) nitrate hexahydrate were each separately dissolved in 20 mL of DIW for 30 min while being constantly stirred. The resultant mixture was designated as S1 after these solutions were heated to 60 °C for 30 min while being vigorously agitated in a beaker. S1 was exposed to 0.154 g of –COOH-modified MWCNTs following their ultrasonographic dispersion in 40 mL of deionized water. Also, 0.5 M NaOH solution was gradually added, dropwise to get the pH down to 10. The reaction mixture was maintained to 80 °C, with continuous stirring, for 5 h, and then allowed to age at room temperature for 24 h. The mixture was filtered, washed four times with hot distilled water, and then oven-dried at 100 °C. The final solid sample was then calcined for 4 h at 350 °C in a muffle furnace and then carefully sealed in a sample vial.

2.4 Instrumentation

For through characterization, the CuO–NiO NC and MWCNTs@CuO–NiO NC were subjected to a number of physico-chemical studies. Using Philips X'Pert apparatus, the crystalline structure was examined by X-ray diffraction (XRD) and the Debye–Scherrer equation was utilized to determine the crystallite sizes. A JEOL JSM-5600LV instrument (Tokyo, Japan) was used for the scanning electron microscopy (SEM) to analyze the microstructure and surface characteristics. A UK INCA-200 instrument was used for the EDX analysis to confirm the elemental composition. FT-IR spectroscopy was used to analyze the surface functional groups in the 4000–400 cm^{-1} range using a Nicolet 560 instrument.

2.5 Photocatalytic assay

The photo-induced degradation of Rh-6G was carried out to evaluate the photocatalytic activity of the CuO–NiO NC and MWCNTs@CuO–NiO NC. First, a stock solution of Rh-6G dye was prepared at a concentration of 15 ppm using distilled water. Then, 20 mg of the synthesized samples was added to 100 mL of this stock solution that had been moved to a reaction vessel. The reaction mixtures were agitated in the dark for half an hour in order to reach adsorption–desorption equilibrium. After exposing the samples to simulated solar light for a predetermined amount of time, the change in the λ-max was observed over a period of time using a double-beam spectrophotometer. The reaction was also performed in the presence of either the catalyst or light under the same reaction conditions to highlight the synergistic effect of both light and the catalyst.

To evaluate the stability and reusability of the prepared photocatalyst, 100 mL of the stock dye solution was treated with 20 mg of the catalyst in the reaction vessel under identical experimental conditions. After each cycle, the catalyst was recovered, and washed and then reused with a fresh dye solution while maintaining the same reaction parameters. This procedure was repeated for five consecutive cycles to assess the catalyst's durability and performance consistency.

2.6 Antibacterial activity assay

The bactericidal behavior of the prepared samples was checked against *E. coli* and *S. aureus* using the agar-well diffusion process. Agar plates were created by dissolving agar nutrients in DIW, and then left to naturally harden at room temperature. Wells were then created in the evenly distributed overnight-cultured bacterial solution on the agar medium using a polystyrene tip. To examine their antibacterial characteristics, stock solutions of the produced nanostructures were created by ultrasonically dispersing varying concentrations (5, 15, 25, and 50 mg) in 5 mL of DIW. These suspensions were then applied to separate wells in amount 100 μL amounts. Following a 24 h incubation period at 37 °C, the antibacterial activity of the synthesized nanostructures was evaluated by estimating the zone of inhibition in millimeters (mm).

2.7 Antioxidant activity assay

Initially, 5 mM potassium persulfate and 14 mM ABTS were mixed in a 12 : 8 (w/w) and 1 : 1 (v/v) ratio to create the $\text{ABTS}^{\bullet+}$ radical cation. The mixture was then left in the dark for 16 h to evaluate its antioxidant activity. The absorbance of the solution was subsequently recorded at 734 nm. Next, 5, 25, 50, 75, 100, and 200 μg of the samples was ultrasonically dispersed in 1 mL of distilled water at room temperature for 30 min. After aging for 30 min, a mixture consisting of 0.2 mL of the synthesized nanostructure suspension and 0.15 mL of $\text{ABTS}^{\bullet+}$ solution was subjected to UV analysis. The optical absorbance of this combination was assessed at 734 nm. Eqn (1) was employed to calculate the percentage of ABTS free radical inhibition, where A_i denotes the absorbance of the sample and A_o refers to the absorbance of the control.

$$\%\ \text{RSA} = \left[\left(\frac{A_\text{o} + A_\text{i}}{A_\text{o}}\right)\right] \times 100 \tag{1}$$

3 Results and discussion

3.1 XRD study

Fig. 1 shows the XRD patterns of CuO–NiO NC and MWCNT-CuO–NiO NC, where the diffraction peaks were assigned to different constituents of the samples. The diffraction peaks at 26.81° and 42.10° were linked to the (002) and (100) planes, as per JCPDS card 00-041-1487, with the prior one corresponding to interlayer spacing and the later one to the in-plane structure of carbon atoms in the hexagonal lattice. The Bragg's reflections at 33.38° and 38.67° were linked with the (110) and (111) planes, corresponding to the reference card 01-080-1916, and were assigned to the monoclinic and space group *Cc* and space number 9. Since the system was a monoclinic system, the length of each of the three coordinates, $a = 4.6927$ Å, $b = 3.4283$ Å and $c = 5.1370$ Å varied, while the two interfacial angles (α and γ) were 90° and β was equal to 99.5460°. The concentration and volume of the crystal lattice unit were 6.48 g cm^{-3} and 81.50×10^3 pm^3, respectively. The diffraction peak at 62.29° was linked with the 220 plane, attributed to the cubic system with the *Fm*3*m* space

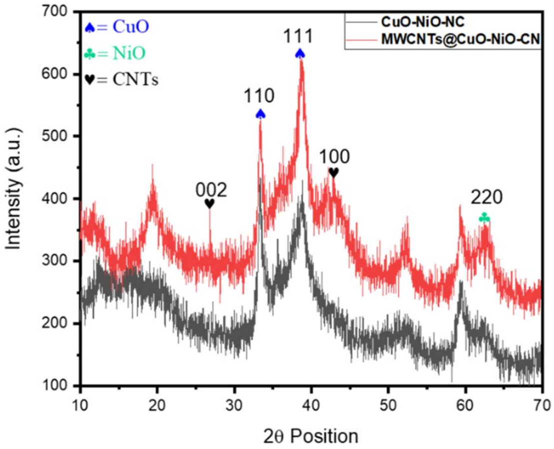

Fig. 1 XRD patterns of the CuO–NiO NC and MWCNTs@CuO–NiO NC.

group and the space number of 225. The three dimensional distance (a, b and c) was 3.1700 Å and all the interfacial angles (α, β and γ) were 90°. The density and volume of the unit cell were 6.84 g cm^{-3} and 71.51 × 10^{3} pm^{3}, respectively.

It was evident from Fig. 1 that both the patterns were much noisier; there might be several reasons to explain this phenomenon. One possibility is that external factors, such as environmental conditions or equipment calibration issues, could be contributing to the increased noise levels. Additionally, variations in the data collection methods may also play a significant role in the discrepancies observed. This might be due to the significant peak broadening of CuO and NiO NPs due to the Scherrer effect, whereby smaller crystallite sizes result in broader and less intense peaks, which can overlap and create a noisy pattern. Moreover, in the composite materials, there were several phases (MWCNTs, CuO, and NiO), where each can contribute its own sets of diffraction peaks. The overlapping of these different sets of peaks may have led to the formation of noisy patterns.

3.2 SEM study

Fig. 2(a) presents the SEM image of the CuO–NiO NC synthesized using the modified sol–gel method. CuO–NiO NC showed a cloudy appearance, which can often result from a combination of particle agglomeration and limited resolution at the surface level. Multiple cavities could have been formed either because of removal of the solvent during the sol–gel method or shrinkage during the drying. Heavy agglomeration occurred because the nanoparticles attracted each other, which is common in metal oxides like CuO and NiO. A dense appearance was noticeable that was due to overlapping particles or aggregated regions that made the material appear more solid. Some elongated or needle-like structures were also obvious in the SEM image and indicated anisotropic growth. Multiple aggregates were a common feature in this nanocomposite, which might have occurred due to hydrolysis and condensation reactions in the sol–gel process. There were also some irregular shapes, which indicated non-homogeneous nucleation and growth during the sol–gel process. The existence of some flaky structures resulted due to solvent evaporation. At this resolution, the porosity was difficult to observe.

When MWCNTs were incorporated into the CuO–NiO NC, significant changes in the composite's morphology were observed, as indicated in Fig. 2(b). The incorporated MWCNTs, with their high surface area and mechanical properties, acted as a scaffold that strongly interacted with the CuO and NiO nanoparticles, consolidating them into a dense, compact structure. A smooth surface could be clearly seen, where the cavities had been minimized to a greater extent. This smooth surface and reduction in cavities occurred because the MWCNTs filled the gaps between the CuO and NiO particles. Agglomeration increased significantly as the MWCNTs and metal oxide particles clustered together due to strong van der Waals forces. The MWCNTs bound the CuO and NiO particles together, creating a unified structure where individual particle boundaries merged into a continuous phase. Bulges were observed on the structure, likely due to MWCNTs or metal oxide nanoparticles clustering, with smaller agglomerates probably forming spheres during drying. The non-porous compact structure resulted from the MWCNTs filling the gaps between nanoparticles, creating a tightly packed, interconnected network that had the appearance of a smooth, homogeneous composite.

3.3 EDX study

The EDX spectrum for both the CuO–NiO NC and MWCNTs@CuO–NiO NC indicated the elements present and their relative concentrations in the samples (Fig. 3a and b). The

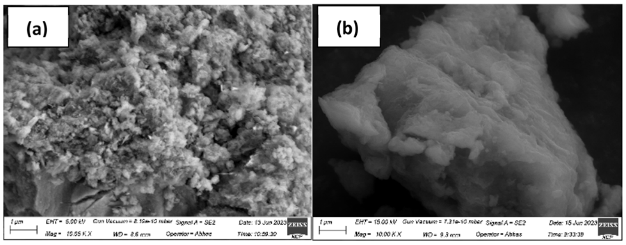

Fig. 2 SEM images of the CuO–NiO NC (a) and MWCNTs@CuO–NiO NC (b).

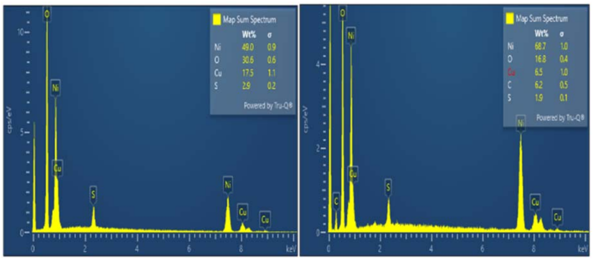

Fig. 3 EDX spectra of the CuO–NiO NC and CNTs-modified CuO–NiO NC.

signal at 0.14 keV revealed the presence of carbon, while the signal at 0.5 keV pointed to oxygen, likely associated with the oxide components of the NCs. The bands at 0.93, 8.1, and 8.9 keV clearly corresponded to copper, while the peaks at 0.81 and 7.5 keV signaled the presence of nickel. The peak at 2.3 keV indicated sulphur. Sulfur in the EDX spectra likely came from impurities in the raw materials, environmental contamination, or the adsorption of atmospheric sulfur, while the carbon signals arose from ambient contamination or handling residues.

Upon incorporating MWCNTs into the CuO–NiO NC, significant changes were observed in the EDX spectrum, including variations in the peak intensities, weight percentages, and atomic percentages of O, C, and Cu. The MWCNTs enhanced the O signals by improving the dispersion of CuO and NiO particles, increasing surface exposure, and facilitating detectability. Similarly, the Cu signals increased as the CNTs prevented particle agglomeration and ensured uniform dispersion. Additionally, the incorporation of CNTs, with their high surface area and conductivity, significantly increased the C content in the matrix, enhancing C exposure and its detection in the EDX spectrum. Conversely, this incorporation of CNTs into the CuO–NiO NC reduced the Ni signals by bonding preferentially with CuO and altering the composite's morphology. A decrease in the S signal intensity occurred due to changes in S chemistry and CNT interactions with CuO/NiO, which suppressed S incorporation. However, the weight and atomic percentages of S increased as the CNTs scattered the X-ray signals, reducing sulfur exposure to the EDX beam.

3.4 EDS mapping

The EDS mapping of the MWCNTs@CuO–NiO NC is presented in Fig. 4, and confirmed the presence of the elemental constituents, *i.e.* Cu, Ni, O, and CNTs. The mapping results revealed a slight agglomeration of Cu, Ni, and O elements, while the CNTs appeared to be monodispersed and uniformly distributed throughout the sample. The presence of Cu, Ni, and O suggested the successful formation of the CuO–NiO nanoparticles, while the C confirmed the incorporation of the MWCNTs. The mapping results indicated there was some degree of agglomeration among the Cu, Ni, and O elements, implying that the metal oxide nanoparticles tended to cluster together. This behavior is commonly observed in nanocomposite synthesis due to the high surface energy of nanoparticles. This observation aligned closely with the SEM results, where the incorporation of MWCNTs was found to enhance agglomeration, likely due to the interaction between the metal oxide nanoparticles and the carbon nanotube surfaces. Moreover, S was detected in the sample, which was attributed to an impurity, which might be due to the use of SDS during the synthetic procedure.

3.5 FT-IR study

The FT-IR spectra of both CuO–NiO NC and CNTs@CuO–NiO NC are presented in Fig. 5. The broad band centered at 3337.57 cm^{-1} along with bands at 3443.32 cm^{-1} as well as 3252.97 cm^{-1} were associated with the tensile collision of H–O–H and hydroxyl incorporation.[25] The weak band at 3013.82 cm^{-1} was contributed to asymmetric C–H stretching.[26] C–H stretching modes of the CNTs appeared at 2936.24 cm^{-1}.[27] A peak at 2929.04 cm^{-1} was attributed to the 2D oscillation mode of the bridging hydroxyl group that was involved in hydrogen bonding with H_2O molecules and surface hydroxyl groups.[28] A minor band appeared at 2365.16 cm^{-1} due to atmospheric CO_2 adsorbed on the surface of the fabricated nanocomposite.[29] In-plane bending of H–O–H coordinated H_2O molecule was responsible for the medium band at 1646.12 cm^{-1}.[30] C=C stretches of the CNTs gave rise to the slightly intense bands at 1613.72 and 1518.95 cm^{-1}.[27,31] C–H bending vibrations were responsible for the weak band at 1477.36 cm^{-1}.[27] The lattice M–OH vibrations were identified as the source of the weak band at 1420.57 cm^{-1},[32] while O–C–O asymmetric vibrations caused the intense band at 1364.95 cm^{-1}.[33] The bands at 1251.81 and 1244.61 cm^{-1}

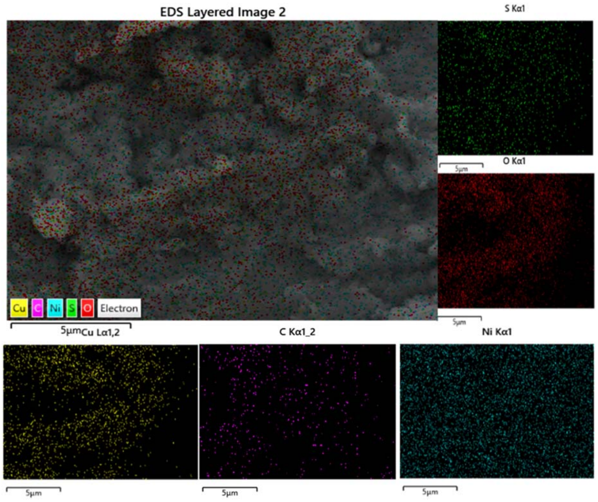

Fig. 4 EDS mapping of the MWCNTs@CuO–NiO NC, showing the presence and distribution of the components in the sample.

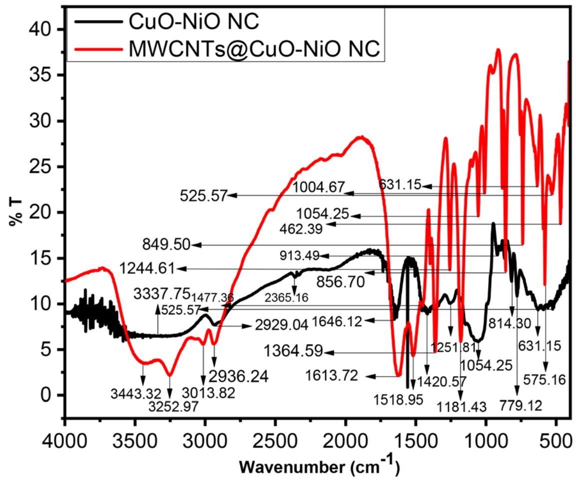

Fig. 5 FT-IR spectra of the CuO–NiO NC and MWCNT-modified CuO–NiO NC.

resulted from O–M–O (M = Cu) vibrations.[34] The intense band at 1181.43 cm^{-1} was caused by C–O bond vibrations.[35] Bands were also observed at 1054.25 cm^{-1} with varying intensities, ascribed to the M–O–M vibrations (where M represents Cu).[34] The band observed at 1004.67 cm^{-1} was generated by the bending vibrations of Cu–O bonds.[36] M–O vibrations (with M = Cu, Ni) produced another weak band at 913.49 cm^{-1}.[37] The out-of-plane C–H deformation mode was responsible for the band at 856.70 cm^{-1},[38] while the band at 849.50 cm^{-1} was ascribed to the M–O–C vibrations.[38] Stretching of Cu–O within the monoclinic lattice led to a band 779.12 cm^{-1}.[39] Bands of different intensities at 631.15 and 575.16 cm^{-1} were produced by Ni–O vibrations.[29,40] The Cu–O stretching vibrations produced bands with distinct intensities at 525.57 cm^{-1}.[34] Cu–O stretching vibrations resulted in another band at 462.39 cm^{-1}.[41] Various changes were observed in the FT-IR spectra of CuO–NiO NC and CNTs@CuO–NiO NC, including variations in the band intensities, the appearance and disappearance of some bands, and enhanced features in the fingerprint region. These changes, resulting from the incorporation of CNTs, were attributed to several scientific factors related to the interactions between the CNTs and the metal oxide matrix, as well as the structural and chemical properties of both materials as described in the following. The introduction of CNTs into the CuO–NiO NC led to new interactions with the metal oxides, altering the bonding environment of the functional groups present in the CuO–NiO NC. This alteration resulted in significant changes in the band intensities. Additionally, the presence of CNTs enhanced the dispersion of CuO and NiO particles within the matrix, which increased the effective surface area and created more active sites for vibrational modes, thereby resulting in increased intensities for certain bands. Moreover, the incorporation of CNTs introduced new vibrational modes due to structural changes and the existence of extra functional groups on the CNT surface. Consequently, some bands became more prominent, while others disappeared. The fingerprint region became more pronounced as a result of the improved interactions between the CNTs and metal oxides, enhancing the vibrational coupling among the different components and leading to stronger, more distinct peaks in this region. Furthermore, the incorporation of CNTs likely induced phase changes or stabilized certain phases in the metal oxide NCs, leading to the emergence of new vibrational signatures that were absent in the pure CuO–NiO NC. These observations underscored the complex interplay between the CNTs and the metal oxide matrix, highlighting the potential for enhanced structural and functional properties in the resulting nanocomposites.

3.6 Photocatalytic study

The CN-NC and MWCNTs@CuO–NiO NC, which were produced using the modified sol–gel process, were tested for assessing their photocatalytic activity against Rh-6G as the test substrate. The catalyst-free degradation of Rh-6G dye was also performed to assess its self-photocatalytic potential. Using natural sunshine, the evaluation was conducted outside from June 3 to June 14, 2024 from 11 a.m. to 3 p.m. The bright brown color of the reaction mixture gradually faded as it underwent deterioration. A rapid decline in the absorbance maximum at 256 nm was seen, indicating that the chromophore responsible for absorbing light at that wavelength had broken down.

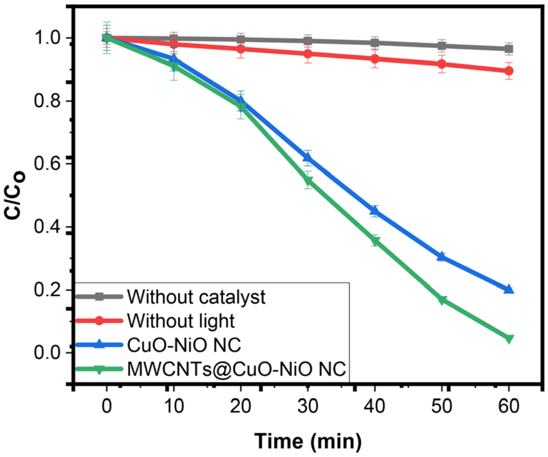

Fig. 6 Rh-6G degradation profile in the presence of the synthesized nanocomposites and sunlight.

In the catalyst-containing samples, this decrease was significant, while it was insignificant in the catalyst-free sample. The peak absorbance gradually decreased over time, as can be seen by the decay curve in Fig. 6. In the initial 20 min, a sharp and substantial decrease in maximum absorption was noted, especially in the sample treated with MWCNTs. However, this was negligible in the catalyst-free sample. After that, the rate of reduction decreased in every sample. The sample that had been altered with MWCNTs showed the biggest decrease in absorbance maximum.

The Rh-6G degradation efficiency was calculated using eqn (1). Fig. 7 illustrates the results, indicating that the CN-NC sample attained 80.09% degradation, while the MWCNTs@CuO–NiO NC sample achieved a superior

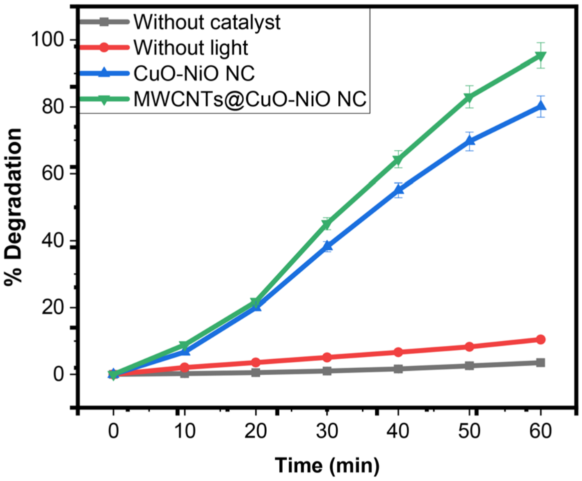

Fig. 7 Degradation efficiency (%) of Rh-6G under solar light catalyzed by the synthesized nanocomposites.

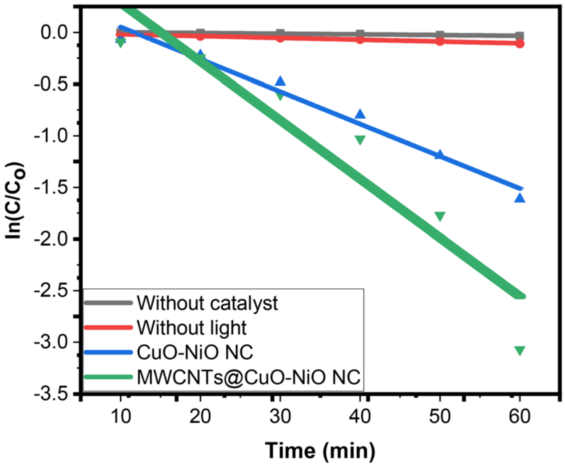

Fig. 8 Kinetic rate constants of the photocatalytic reactions mediated by the synthesized nanocomposites.

degradation level of 95.37%. In the control experiments, the photocatalytic reaction was conducted with only light (no catalyst) or only catalyst (no light), resulting in 3.52% and 10.45% degradations, respectively. These findings highlighted the varying effectiveness of each sample in breaking down Rh-6G under the given experimental conditions. Among all the tested samples, the MWCNTs@CuO–NiO NC demonstrated the highest photocatalytic performance, while the absence of a catalyst resulted in minimal activity.

The deterioration rate constants for the light-induced reactions, calculated using eqn (2), were 0.02737, 0.0477, and 5.99312 min^{-1} for CN-NC, MWCNTs@CuO–NiO NC, and the catalyst-free sample, respectively (Fig. 8). These values provided a simplified understanding of Rh-6G degradation under the specified conditions, providing an analysis of the photocatalytic performance of each sample. Generally, a faster breakdown process and hence higher photocatalytic efficacy are indicated by a greater rate constant. The findings revealed that MWCNTs@CuO–NiO NC achieved the highest rate constant of 0.0477 min^{-1}, indicating its efficiency in facilitating degradation of the target compound relative to the other samples.

The photocatalytic activity index (PAI) is a quantitative index used to compare the efficacy of different photocatalysts under given conditions, including the degradation rate, utilized catalyst dose, and light intensity, enabling fair comparisons between different catalysts. The PAI can be calculated using eqn (2), where k is the rate constant (min^{-1}), m is the mass of catalyst (mg) and I is the light intensity (mW cm^{-2}). The calculated PAIs were 0.13×10^{-4} and 0.22×10^{-4} for the CuO–NiO NC and MWCNTs@CuO–NiO NC, respectively. The PAI values clearly suggest that the integration of MWCNTs significantly improved the photocatalytic activity of the composite material.

$$\text{PAI} = k/(m \times I) \tag{2}$$

3.6.1 Proposed mechanism. Rh-6G is a xanthene dye with a complex structure and its degradation proceeds through a series of steps involving the attack of generated $^{\bullet}$OH and ROS, leading to decolorization and eventual mineralization. When the catalyst absorb solar light, the valence electron (e^-) are excited into the conduction band (CB) and a positive hole (h^+) is generated in the valence band (VB). The h^+ react with $^-OH/H_2O$ to generate $^{\bullet}$OH attached on the ethyl group and xanthene ring. At the same time, the excited e^- react with oxygen, leading to the formation of ROS species, which are responsible for the breakage of the conjugated bonds. The N-de-ethylation is the initial and most prominent step in the degradation of Rh-6G, where the highly reactive $^{\bullet}$OH radicals attack the ethyl groups attached to the nitrogen atoms of the xanthene core, generating a series of *N*-de-ethylated intermediates, which are responsible for the initial decolorization the solution. Further attack by ROS on the xanthene ring structure leads to the breakage of the conjugated double bonds, while electrophilic attack by $^{\bullet}$OH on the aromatic rings leads to the formation of smaller aromatic fragments. Further oxidative attacks by the ROS lead to the breakage of C–C, C–N and C–O bonds, and results in the formation of simpler molecules like H_2O, CO_2, NH_4^+ and NO_3^-.

3.7 Factor interactions in photocatalytic optimization

3.7.1 Effect of the pH. To test the effect of the pH, 0.1 M NaOH and a 0.1 M HCl solutions were utilized to adjust the pH of the Rh-6G solution. Changes in the solution's pH have an impact on the proportion of H^+ and OH^-, which produce free radicals that degrade Rh-6G dye. Close observation was made of how the pH variations affected the percentage rate of deterioration (Fig. 9). The breakdown rates determined by the study were 56.02% at pH 4, 69.83% at pH 5, 83.29% at pH 6, 95.37% at pH 7, 85.02% at pH 8, and 72.17% at pH 9. According to the findings, the rate of degradation rose as the pH increased, peaking at neutral pH, and then began to decrease at higher pH values. There are two types of Rh-6G: ionic ($R6G^+$) and non-ionic (R6G). Higher solution pH causes the cationic dye molecules to change into neutral forms, which prevents neutral dye molecules from interacting attractively with the CuO–NiO nanocomposite's negatively charged surface. Consequently, photocatalytic degradation decreased above pH 7. Also, the

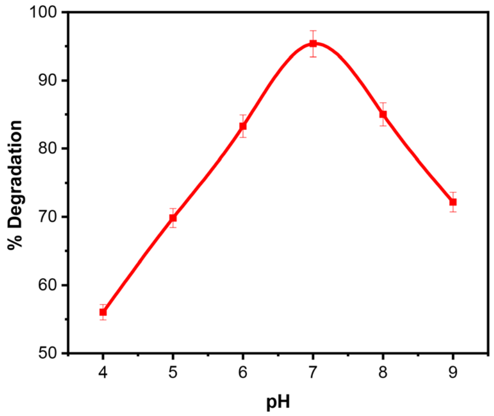

Fig. 9 pH-dependent photocatalytic degradation efficiency of the synthesized nanocomposites.

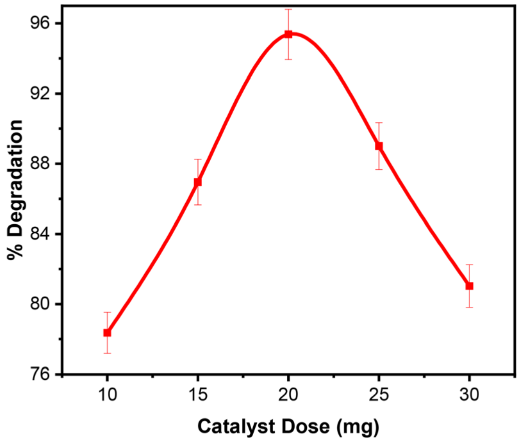

Fig. 10 Effect of catalyst concentration (mg L^{-1}) on Rh-6G degradation efficiency.

protonation of nitrogen in the secondary amine group of the xanthene ring causes cationic dye molecule to change into a hydrophilic one below pH 7. This hydrophilic nature lowers the effective catalytic activity because it produces fewer radicals than under neutral pH 7 circumstances. As a result, the acidic pH range showed less photocatalytic degradation.[42]

3.7.2 Dose optimization. Fig. 10 illustrates the degradation of Rh-6G under different catalyst concentrations (10 to 30 mg). The results showed that when the catalyst dosage was increased, the percentage degradation rose correspondingly. The higher the catalyst concentration, the faster the dye degraded.[43] The highest activity was seen at a 20 mg catalyst loading, indicating that this was the ideal photocatalyst dosage for the MWCNT-modified CuO–NiO NC photocatalytic process. With a higher dose of the NC, the overall surface area expanded, increasing the number of binding sites available for interaction with the dye. The degradation percentage of Rh-6G increased from 78.36% to 95.37% with the rise in the MWCNTS@CuO–NiO NC concentration from 10 to 20 mg. Degradation, however, dropped to 89.01% at 25 mg and then to 81.03% at 30 mg. This improved degradation at higher catalyst concentration was likely due to the increased surface area of NC, which provided more active sites for dye interaction.[44] The degradation was improved by the production of highly reactive species when the density of the active sites on the NCs rose. A reduced decomposition of the dye, however, indicated the production of transistor byproducts at the higher dosages of 25 and 30 mg. Furthermore, the NCs may accumulate at higher concentrations, which could result in less breakdown. This decline may also be caused by decreased photon interactions at the catalyst interface and less efficient photon absorption.[45–47]

3.7.3 Effect of the initial concentration. Using five different starting catalyst concentrations (5–25 ppm), the light-induced decomposition of Rh-6G was examined; the resulting percentage degradation rates were 73.42%, 84.26%, 95.37%, 87.16%, and 76.97%, respectively (Fig. 11). The rate of dye degradation increased noticeably once the initial concentrations hit 15 ppm. Nevertheless, the proportion of degradation decreased as the solution strength increased further. The highest degradation efficiency of 95.37% demonstrated that an initial concentration of 15 ppm was the optimal condition for the enhanced photoreactivity.

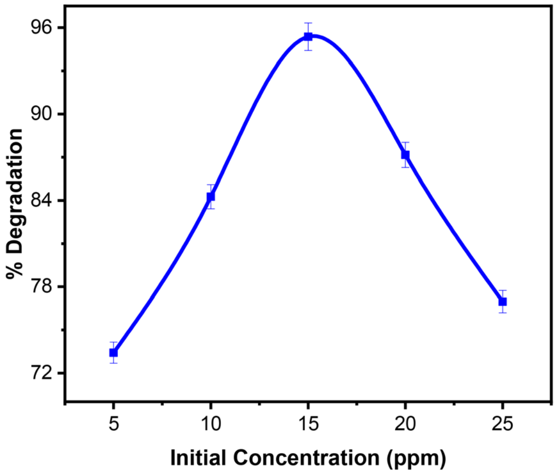

Fig. 11 Comparative photocatalytic performance across different initial catalyst concentrations.

The reduced degradation was an outcome of MWCNTs@CuO–NiO NC's reactive centers becoming fully filled and saturated at higher concentrations. Elevated concentrations that interfere upon photoirradiation can lead to decreased hydroxyl ion generation and, thus, decreased photocatalytic effectiveness. This decline may also be due to the generation of reactive intermediates that compete with Rh-6G for available binding sites on the NC surface.

3.7.4 Reusability effects. The durability of MWCNTs@CuO–NiO NC as a photocatalyst under prolonged exposure is a crucial factor. To assess its stability, the NC underwent five consecutive reuse cycles, which showed degradation percentages of 95.37%, 88.34%, 81.69%, 75.04%, and 61.21%, for cycles 1 through 5, respectively (Fig. 12). The high initial degradation efficacy (95.37%) was likely due to the fresh catalyst form, which offered an optimal quantity of binding sites. Surface contaminants, slight structural changes, or early

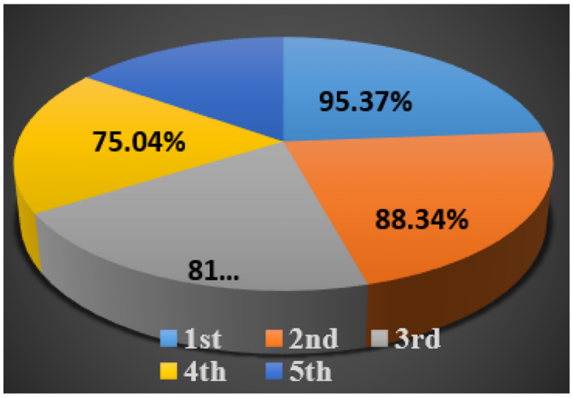

Fig. 12 Recycling efficacy of the MWCNTs@CuO–NiO NC.

catalyst deactivation could all be blamed for the progressive decline in efficacy. The activity rate can experience a gradual decline as the catalytic activity and dye attached to the photocatalyst are lost during the regeneration process.[42] Moreover, during reuse, contaminants from the reaction conditions can accumulate at the catalyst interface, reducing the catalytic effectiveness. Agglomeration, structural changes, and loss of active molecules are some of the elements that might deactivate a catalyst over time, lowering the number of interactions sites that are accessible for reactions triggered by radiant energy.

3.8 Antibacterial activity

Using the agar-well diffusion method, the synthetic materials' antibacterial activity was evaluated, and the findings are shown in Fig. 13. The CuO–NiO NC exhibited high antibacterial activity against both *S. aureus* (Gram-positive) and *E. coli* (Gram-negative) bacteria. *E. coli* was found to be more resistant to both nanocomposites compared to *S. aureus*, which was consistent with the general trend that Gram-negative microbes are often more fortified to bacteriostatic agents because of their external layer structure. The activity of the CuO–NiO NC was found to be higher than that of the standard drug, indicating its potential as an effective antibacterial agent. The solvent used in the experiments did not interfere with the antibacterial activity of the samples, confirming that the observed effects were solely due to the nanocomposites. Interestingly, the MWCNTs@CuO–NiO nanocomposite showed reduced antibacterial activity compared to the bare CuO–NiO NC. Despite the reduction, the MWCNTs@CuO–NiO NC still demonstrated significant antibacterial activity, though it was lower than that of the standard drug. The incorporation of MWCNTs may shield or block the active sites of CuO–NiO nanoparticles, reducing their direct interaction with bacterial cells. The presence of MWCNTs could lead to the agglomeration of CuO–NiO nanoparticles as was evident from the SEM images, reducing their effective surface area and, consequently, their antibacterial activity. The incorporation of MWCNTs alter the surface chemistry of the metal oxides as the metal ions bind to functional sites on the MWCNTs, which may reduce the metal oxides affinity for bacterial cell walls, thereby decreasing its effectiveness.

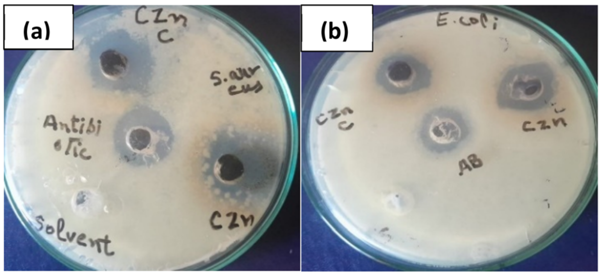

Fig. 13 Experimental photographs showing the antibacterial activity of the CuO–NiO NC and MWCNTs@CuO–NiO NC against *S. aureus* (a) and *E. coli* (b).

3.9 Antioxidant activity

The antioxidant activities of CuO–NiO NC and MWCNTs@CuO–NiO NC were assessed against ABTS$^{\bullet+}$ solution and contrasted with vitamin C as a reference. Table 1 displays the findings. A solution containing ABTS$^{\bullet+}$ was added to ascorbic acid and the synthesized samples at various concentrations of 5, 25, 50, 100, 200, and 400 μg mL^{-1} in order to assess the percentage radical scavenging activity. The antioxidant activity of both samples increased with the increasing concentrations, indicating that more antioxidants were required to deactivate the ABTS$^{\bullet+}$ radical cations.[45,46] The percentage radical scavenging activity rose as the concentration rose. At different concentrations, CuO–NiO NC exhibited scavenging activity from 22.076% to 82.336%, whereas MWCNTs@CuO–NiO NC showed scavenging activity ranging from 24.14% to 90.924%. The anionic NCs' donor surface, which may be responsible for trapping the ABTS free radical species, may account for both NCs' antioxidant activities,[46,47] and higher antioxidant activity may have occurred because it could combine more reactive oxygen species.[34] A higher proportion of NPs was shown to enhance the ABTS free radicals scavenging activity, which was explained by the fact that there were no more NPs accessible to interact with the ABTS free radicals.[48] The antioxidant concentration that neutralize 50% of the ABTS$^{\bullet+}$ radical cations is known as IC$_{50}$. CuO–NiO NC's IC$_{50}$ value was determined to be 116.52 μg mL^{-1}. The IC$_{50}$ value for MWCNTs@CuO–NiO NC was 84.61 μg mL^{-1}, whereas it was 92.74 μg mL^{-1} for ascorbic acid. Determining the standard deviation helps evaluate consistency by showing how antioxidant activity data vary from the mean. A lower standard deviation indicates that the results are highly accurate and consistent. Greater variability is shown by a bigger standard deviation, which implies that the antioxidant activity levels are less consistent. For CuO–NiO NC, MWCNTs@CuO–NiO NC, and ascorbic acid, the corresponding values were 1.68, 1.69, and 1.75, suggesting that CuO–NiO NC produced the most accurate and consistent findings. Variance is a measure of the variability of antioxidant activity measurements; it is the square of the standard deviation and mean squared variation from the mean. A greater variance indicates that samples or experimental settings differ more in terms of antioxidant activity. The CuO–NiO NC, MWCNTs@CuO–NiO NC, and ascorbic acid had variance values of 2.82, 2.84, and 3.09, respectively. According to these findings, the antioxidant activity of CuO–NiO NC varied the least among the samples and different circumstances. The CuO–NiO NC, MWCNTs@CuO–NiO NC, and ascorbic acid were shown to have a dose and %RSA correlation of 0.098, 0.108, and 0.102, respectively. According to this, ascorbic acid had the highest correlation, with higher dosages of MWCNTs@CuO–NiO NC being linked to a higher %RSA while higher doses of ascorbic acid were not. The MWCNT incorporation facilitated efficient electron transfer, augmented the active sites, and stabilized the reactive species, enhancing the composite's antioxidant performance. The CuO–NiO NC further exploited SPR effects, redox cycling, and metal–ligand interactions to scavenge free radicals and reduce oxidative stress.

Table 1 Antioxidant activity of the synthesized NCs against ABTS free radicals

Samples	Concentration (μg mL^{-1})	%RSA	IC$_{50}$ (μg mL^{-1})	Variance (S^2)	Standard deviation (S)	Correlation between dose and %RSA
CuO–NiO NC	5	22.076				
	25	30.188				
	50	43.228				
	100	59.916	116.82	2.82	1.68	0.098
	200	74.004				
	400	82.3366				
MWCNT@CuO–NiO NC	5	24.144				
	25	33.432				
	50	49.796				
	100	65.124	84.61	2.84	1.69	0.108
	200	79.612				
	400	90.924				
Ascorbic acid	5	21.92				
	25	33.58				
	50	47.956				
	100	57.396	92.74	3.09	1.75	0.102
	200	83.976				
	400	94.068				

4. Conclusions

In this study, CuO–NiO NC and MWCNTs@CuO–NiO NC were successfully synthesized by following a simple, user friendly and cost-effective sol–gel protocol. The noisy XRD patterns obtained were evidence of amorphous content in the samples along with crystalline phase, which was expected due to the low-temperature system used in the synthetic procedure. Upon the incorporation of MWCNTs, the morphology of the CuO–NiO NC completely changes and the particles surfaces were covered by CNTs. The bactericidal results demonstrated the superior antibacterial activity of the CuO–NiO NC compared to the MWCNTs@CuO–NiO NC and the standard drug, wherein the incorporation of MWCNTs reduced the activity due to factors such as shielding the active sites, the altered surface chemistry, and agglomeration. However, beside this, the MWCNTs@CuO–NiO NC still retained significant antibacterial properties against both tested bacteria (*E. coli* and *S. aureus*). However, the antioxidant activity increased upon the interaction of MWCNTs with the CuO–NiO NC and the IC$_{50}$ was found to be lower than that of ascorbic acid, demonstrating the high potential of the composite. The promising photocatalytic and antibacterial efficacies of the CuO–NiO and MWCNTs@CuO–NiO NCs motivates us to further explore their (i) green hydrogen production *via* water splitting, (ii) solar cell integration, and (iii) *in vivo* biomedical applications, contingent on rigorous toxicity assessments.

Data availability

All relevant experimental details and raw data, including characterization results (XRD, SEM, FTIR, EDX AND EDS-mapping) and photocatalytic, antibacterial, and antioxidant activity measurements, have been archived and can be accessed by request. The data that support the findings of this study are available from the corresponding author upon reasonable request. Any additional information regarding the materials and methods used in this study can also be provided upon request to support further inquiries and reproduction of results.

Author contributions

Amjad Latif Lone-formal analysis and writing-original draft; Sadiq Ur Rehman-supervision and project administration; Sirajul Haq-conceptualization, methodology and project administration; Shafia Shujaat–visualization and writing-original draft; Afrah F. Alkhuriji, and Nawal M. Al-Malahi–software, validation and funding acquisition; Abdus Samad and Jamoliddin Razzokov-data curation and writing–review & editing.

Conflicts of interest

There are no conflicts to declare associated with this manuscript.

Acknowledgements

The authors extend their appreciation to the Ongoing Research Funding program (ORF-2025-97), King Saud University, Riyadh, Saudi Arabia.

Notes and references

1 P. Yadav, K. Usha and B. Singh, in *Climate Change and Crop Stress*, Elsevier, 2022, pp. 271–298.

2 V. C. Pandey and V. Singh, *Exploring the Potential and Opportunities of Current Tools for Removal of Hazardous Materials from Environments*, Elsevier Inc., 2019.

3 M. Zain, K. A. Yasin, S. Haq and A. Syed, *Mater. Res. Bull.*, 2024, **11**(4), 045002.

4 M. Farhan Hanafi and N. Sapawe, *Mater. Today: Proc.*, 2020, **31**, A141–A150.

5 S. Yadav, K. Shakya, A. Gupta, D. Singh, A. R. Chandran, A. Varayil Aanappalli, K. Goyal, N. Rani and K. Saini, *Environ. Sci. Pollut. Res.*, 2023, **30**, 71912–71932.

6 M. Zain, K. A. Yasin, S. Haq, W. Rehman, S. U. Din, S. Shujaat, A. Syed, M. K. Hossain, B. A. Paray, J. Razzokov and A. Samad, *RSC Adv.*, 2024, **14**, 15085–15094.

7 M. Ismail, K. Akhtar, M. I. Khan, T. Kamal, M. A. Khan, A. M. Asiri, J. Seo and S. B. Khan, *Curr. Pharm. Des.*, 2019, **25**, 3645–3663.

8 N. S. Bhaskar, A. D. Kadam, J. J. Biwal, P. M. Diwate, R. R. Dalbhanjan, D. D. Mahale, S. P. Hinge, B. S. Banerjee, A. V. Mohod and P. R. Gogate, *Desalin. Water Treat.*, 2016, **57**, 18275–18285.

9 B. Almutairy, *Front. Microbiol.*, 2024, **15**, 1381511.

10 R. Khan, B. Islam, M. Akram, S. Shakil, A. Ahmad, S. M. Ali, M. Siddiqui and A. U. Khan, *Molecules*, 2009, **14**, 586–597.

11 M. Terreni, M. Taccani and M. Pregnolato, *Molecules*, 2021, **26**(9), 2671.

12 A. Shah, S. Haq, W. Rehman, W. Muhammad, S. Shoukat and M. ur Rehman, *Mater. Res. Express*, 2019, **6**, 045045.

13 R. Van Wijk, E. P. A. Van Wijk, F. A. C. Wiegant and J. Ives, *Indian J. Exp. Biol.*, 2008, **46**, 273–309.

14 L. A. Pham-Huy, H. He and C. Pham-Huy, *Int. J. Biomed. Sci.*, 2008, **4**, 89.

15 B. B. Mathew, A. Tiwari and S. K. Jatawa, *J. Pharm. Res.*, 2011, **4**, 4340–4343.

16 U. Younas, A. Gulzar, F. Ali, M. Pervaiz, Z. Ali, S. Khan, Z. Saeed, M. Ahmed and A. A. Alothman, *Water*, 2021, **13**(19), 2653.

17 M. Anjum, R. Miandad, M. Waqas, F. Gehany and M. A. Barakat, *Arab. J. Chem.*, 2019, **12**, 4897–4919.

18 P V Baptista, M. P. McCusker, A. Carvalho, D. A. Ferreira, N. M. Mohan, M. Martins and A. R. Fernandes, *Front. Microbiol.*, 2018, **9**, 1441.

19 S. Dubey, T. Virmani, S. K. Yadav, S. Ashwani, K. Girish and A. Abdulsalam, *J. Nanomater.*, 2024, 9914079.

20 N. A. S. Ridha, H. K. Egzar and N. M. Kamal, *AIP Conf. Proc.*, 2020, **2290**(1), 1–7.

21 T. A. T. N. Hendawy, S. El Rabaie, A. Esmat and M. K. El Mansy, *Polym. Bull.*, 2019, **76**, 4769–4784.

22 S. Thota, J. H. Shim and M. S. Seehra, *J. Appl. Phys.*, 2013, **114**(21), 1–5.

23 K. Kumar, R. Kumar, R. Jasrotia, S. Kalia, V. Arya and A. Kumar, *Discover Appl. Sci.*, 2024, **6**(3), 87.

24 Y. He, J. Qian, P. Wang, T. Xie, D. D. Dionysiou, B. Lu and S. Tang, *Appl. Catal. B Environ.*, 2023, **330**, 122620.

25 S. A. Moon, B. K. Salunke, B. Alkotaini, E. Sathiyamoorthi and B. S. Kim, *IET Nanobiotechnol.*, 2015, **9**, 220–225.

26 S. Haq, M. Rashid, F. Menaa, N. Shahzad, M. Imran, S. Y. M. Alfaifi, O. Madkhali, M. D. Aljabri, M. Ashravi, R. A. Tayeb and M. M. Rahman, *Arab. J. Chem.*, 2023, **16**, 104917.

27 M. Bahgat, A. A. Farghali, W. M. A. El Rouby and M. H. Khedr, *J. Anal. Appl. Pyrolysis*, 2011, **92**, 307–313.

28 M. Takeuchi, L. Bertinetti and G. Martra, *Appl. Catal., A*, 2006, **307**(1), 13–20.

29 S. Haq, A. W. Raja, S. U. Rehman, A. Mezni, M. Ben Ali, A. Hedfi, M. I. Shahzad, W. Rehman, N. Shahzad, M. Waseem and P. Ahmad, *J. Chem.*, 2021, **2021**(1), 3475036.

30 A. Ragunathan, R. Krishnan and B. Ameen, *J. Chem. Res.*, 2015, **39**, 622–626.

31 S. C. Her and C. Y. Lai, *Materials*, 2013, **6**(6), 2274–2284.

32 A. Sinha, V. Nand, B. Raj and S. Kumar, *J. Hazard. Mater.*, 2011, **192**, 620–627.

33 T. Waheed, P. Min, S. Shujaat, S. Haq and M. K. Hossain, *Desalin. Water Treat.*, 2024, **319**, 100495.

34 A. Hamid, S. Haq, S. Ur Rehman, K. Akhter, W. Rehman, M. Waseem, S. Ud Din, Z. U. Abdin, M. Hafeez, A. Khan and A. Shah, *Chem. Pap.*, 2021, **75**, 4189–4198.

35 L. Stobinski, B. Lesiak, L. Kövér, J. Tóth, S. Biniak, G. Trykowski and J. Judek, 2010, **501**, 77–84.

36 M. A. Wahba and A. A. Badawy, *J. Sol-Gel Sci. Technol.*, 2020, **94**, 637–647.

37 P. L. Meena, K. Poswal, A. K. Surela and J. K. Saini, 2021, **84**, 2615–2634.

38 T. Oh, *Bull. Korean Chem. Soc.*, 2009, **30**(2), 467–470.

39 F. U. Rehman, R. Mahmood, M. B. Ali, A. Hedfi, M. Almalki, A. Mezni, W. Rehman, S. Haq and H Afsar, *Materials*, 2021, **14**(20), 6085.

40 S. U. Din, H. Iqbal, S. Haq, P. Ahmad, M. U. Khandaker, H. O. Elansary and T. K. Z. El-Abedin, *Crystals*, 2022, **12**(2), 146.

41 R. Dobrucka, *J. Inorg. Organomet. Polym. Mater.*, 2018, **28**, 812–819.

42 J. Ren, Y. Z. Wu, Y. Dai, D. W. Sha, M. Chen, J. J. Wang, J. M. Pan, H. Tang, X. N. Cheng and X. H. Yan, *Mater. Technol.*, 2017, **32**, 574–583.

43 U. G. Akpan and B. H. Hameed, *J. Hazard. Mater.*, 2009, **170**, 520–529.

44 D. M. Nzilu, E. S. Madivoli, D. S. Makhanu, S. I. Wanakai, G. K. Kiprono and P. G. Kareru, *Sci. Rep.*, 2023, **13**, 14030.

45 B. Siripireddy and B. K. Mandal, *Adv. Powder Technol.*, 2017, **28**, 785–797.

46 M. A. El-Bindary, M. G. El-Desouky and A. A. El-Bindary, *Appl. Organomet. Chem.*, 2022, **36**, 1–16.

47 M. Afifi, O. A. Almaghrabi and N. M. Kadasa, *BioMed Res. Int.*, 2015, **2015**(1), 153573.

48 S. A. Bhat, F. Zafar, A. H. Mondal, A. Kareem, A. U. Mirza, S. Khan, A. Mohammad, Q. M. R. Haq and N. Nishat, *J. Iran. Chem. Soc.*, 2020, **17**, 215–227.